Using colloidal deposition to mobilize immiscible fluids from porous media

Joanna Schneider ⓘ, Rodney D. Priestley, and Sujit S. Datta ⓘ*

Chemical and Biological Engineering, Princeton University, Princeton, New Jersey 08544, USA

Colloidal particles hold promise for mobilizing and removing trapped immiscible fluids from porous media, with implications for key energy and water applications. Most studies focus on accomplishing this goal using particles that can localize at the immiscible fluid interface. Therefore, researchers typically seek to optimize the surface activity of particles, as well as their ability to freely move through a pore space with minimal deposition onto the surrounding solid matrix. Here, we demonstrate that deposition can, surprisingly, promote mobilization of a trapped fluid from a porous medium without requiring any surface activity. Using confocal microscopy, we directly visualize both colloidal particles and trapped immiscible fluid within a transparent, three-dimensional porous medium. We find that as nonsurface active particles deposit on the solid matrix, increasing amounts of trapped fluid become mobilized. We unravel the underlying physics by analyzing the extent of deposition, as well as the geometry of trapped fluid droplets, at the pore scale: deposition increases the viscous stresses on trapped droplets, overcoming the influence of capillarity that keeps them trapped. Given an initial distribution of trapped fluid, this analysis enables us to predict the extent of fluid mobilized through colloidal deposition. Taken together, our work reveals a new way by which colloids can be harnessed to mobilize trapped fluid from a porous medium.

I. INTRODUCTION

Studies of colloidal particles in porous media inform their use in broad applications [1] including groundwater remediation [2,3] and enhanced oil recovery (EOR) [4–6]. The ability to predict whether and how nano- and microscale particles can help mobilize trapped immiscible fluids from a heterogeneous pore space is critically important in both of these applications. For example, nonaqueous contaminants in groundwater aquifers pose a major risk to human health [7,8]; the widespread use of organic compounds as industrial solvents along with improper disposal have caused them to infiltrate aquifers, where they remain trapped by capillarity [9]. Thus, remediation efforts are exploring the use of colloidal particles to help mobilize these contaminants [10–12]. Another example is that of oil recovery: while primary and secondary recovery processes are commonly employed, they still leave up to 90% of the oil in a subsurface reservoir behind, again due to trapping by capillarity [13]. As global energy demand rises, researchers are therefore increasingly exploring the use of colloidal particles to help mobilize trapped oil for enhanced recovery [14–17].

One mechanism by which colloidal particles are thought to mobilize trapped immiscible fluid is through surface activity. In this mechanism, particles preferentially localize at immiscible fluid-fluid interfaces owing to their surface chemistry, thereby reducing the interfacial tension and weakening the capillary stresses that keep fluid trapped [4,11,18–22]. Nonsurface active colloids also have potential for immiscible fluid mobilization, for example, through their ability to reduce fluid slip

---

*To whom correspondence should be addressed: ssdatta@princeton.edu

[23] or enhance disjoining pressure via the formation of thin films [6,24]. Importantly, all of these mechanisms rely on the ability of colloidal particles to freely move through the heterogeneous pore space without depositing on the solid matrix: deposition hinders the ability of particles to localize at target fluid interfaces, [2,25], and potentially causes clogging that impedes subsequent flow [26–29]. As a result, researchers typically seek to minimize deposition of colloidal particles in porous media, for example, by tuning colloidal interactions or only using low concentrations of particles [30,31].

Here, we demonstrate that deposition can, surprisingly, promote mobilization of a trapped immiscible fluid from a three-dimensional (3D) porous medium without requiring surface activity. We do this by using refractive index matching to render the medium transparent, which enables us to simultaneously visualize colloidal deposition and immiscible fluid droplets within the pore space. As the particles deposit on the solid matrix under an imposed flow rate, increasing amounts of trapped fluid become mobilized, ultimately enabling removal of ∼70% of the fluid. By analyzing the extent of deposition, as well as the geometry of trapped fluid droplets at the pore scale, we determine that deposition reduces the permeability of the medium, thereby enabling the viscous stresses on the trapped droplets to overcome the influence of capillarity keeping them trapped without excessively restricting the fluid flow. We develop a geometric model that quantifies changes in the permeability due to particle deposition, providing a first step toward predicting the extent of fluid mobilization given any initial distribution of trapped fluid. Our work reveals that colloidal deposition can be harnessed to mobilize trapped immiscible fluids and provides quantitative guidelines for applying this new mechanism.

II. ESTABLISHMENT OF AN INITIAL TRAPPED FLUID CONFIGURATION

We prepare a model 3D porous medium by lightly sintering a dense packing of borosilicate glass beads at $1000\,°C$ for 3.5 min in a quartz capillary tube with a square cross-sectional area $A = 9$ mm^2. The beads have radii $a = 62–75\ \mu$m and the packing spans a length $\ell = 2.6$ cm. Light scattering from the solid matrix formed by the beads typically renders the medium opaque, precluding imaging of flow and transport in the pore space. To overcome this limitation, we formulate a wetting fluid of 50 wt% dimethyl sulfoxide (DMSO), 30 wt% glycerol, and 20 wt% deionized water, dyed with Rhodamine Red, that has the same refractive index as the solid matrix; thus, infiltrating the pore space with this fluid renders the medium completely transparent. Furthermore, this fluid enables the colloidal particles used in our experiment to remain stable in suspension over an experimental time scale of >18 h, as verified by confocal microscopy at single-particle resolution. To investigate immiscible fluid trapping and mobilization, we formulate another fluid, an oily mixture of aliphatic and aromatic hydrocarbons (Cargille refractive index liquids), which has the same refractive index as the wetting fluid and the solid matrix, but is nonwetting. Measurements performed on a similar fluid pair indicate that the three-phase contact angle between the wetting fluid and glass in the presence of the nonwetting oil is $\theta \approx 5\,°$ [32]. The interfacial tension between the two liquids is $\gamma \approx 13$ mN/m as measured previously [33] and the dynamic shear viscosities of the wetting and nonwetting fluids are $\mu_w = 10.8$ mPa s and $\mu_{nw} = 16.8$ mPa s, respectively, measured using a cone-plate rheometer. Before saturating the pore space with fluid, we pull vacuum and push CO_2 through the medium. We then saturate the pore space with deionized water to dissolve any remaining CO_2. Finally, we pull vacuum once more before saturating the pore space with the dyed particle-free wetting fluid, preventing trapping of any residual air bubbles in the medium.

We then use a Nikon A1R+ confocal fluorescence microscope to characterize the pore space structure, as schematized in Fig. 1(a). Specifically, we obtain images, each spanning 1,024 μm × 1,024 μm in the xy plane at a single depth within the porous medium centered at $z = 135\ \mu$m, with an optical thickness of 14 μm. A magnified view from one image is shown in Fig. 1(b). The brightness in the image reflects the fluorescent signal from the dyed wetting fluid in the pore space, with primary excitation and emission at 560 and 580 nm, respectively, enabling identification of the glass beads by their contrast with the dyed wetting fluid and shown by the dark circles in the bottom of the image. Together, the tiled images span the entire cross section of the medium and therefore
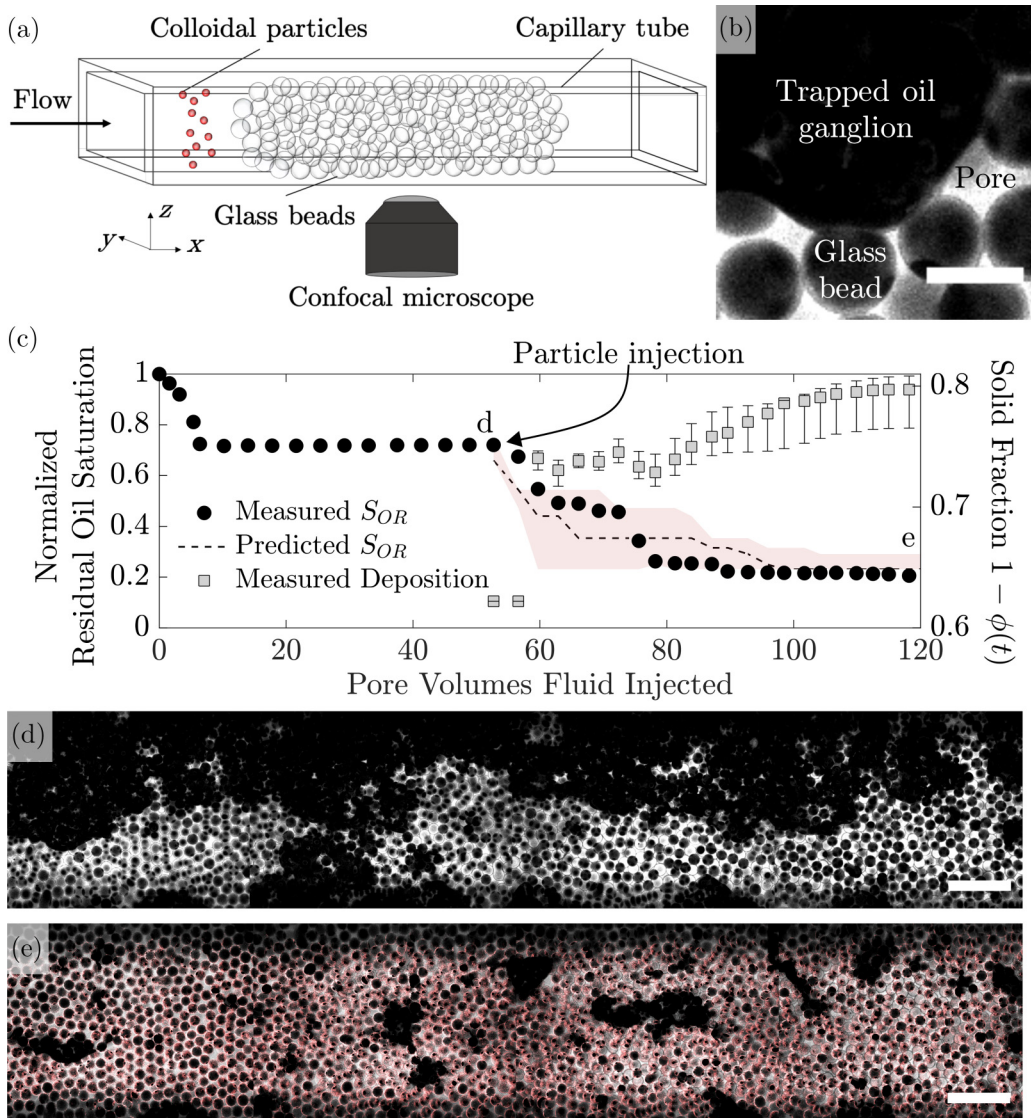
FIG. 1. Colloidal deposition promotes oil mobilization. (a) Schematic of the porous medium composed of glass beads packed in a capillary tube. Fluid flow is imposed along $+x$ and micrographs are taken at a fixed depth z within the medium. (b) Magnified micrograph showing trapped oil before particles are injected. Fluorescent signal from the dyed wetting fluid appears as white; hence, white indicates pore space, black circles show the beads, and additional black shows a trapped oil ganglion. Scale bar represents 150 μm. (c) Black points show the variation of the residual oil saturation S_{OR}, normalized by its maximal value 0.75, over the course of the experiment. Injecting particle-free wetting fluid results in an initial slight decrease in S_{OR}. We then inject the particle suspension at the time indicted by the arrow, which results in a further decrease in S_{OR}. Gray points show the increase in the solid fraction $1 - \phi(t)$ over time due to deposition measured from the micrographs. Error bars show differences in the calculated solid area fraction for $\pm 20\%$ of the image binarization threshold. Dashed line shows our theoretical prediction of S_{OR}, and the red region shows uncertainty in the prediction arising from heterogeneities in deposition as described in Fig. 4. (d) and (e) Images of the porous medium before and after colloidal injection, respectively, as indicated in (c), showing that particle deposition—indicated by red—mobilizes trapped oil. Scale bars represent 750 μm. Imposed flow direction is from left to right.

reproduce a two-dimensional (2D) slice of the pore space. Using adaptive binarization of the images and restricting all analysis to ≈ 5 bead diameters away from the inlet and outlet to minimize the influence of boundaries, we measure the initial porosity of the pristine medium, $\phi_0 = 0.38 \pm 0.06$, in good agreement with previous measurements [32].

We introduce the nonwetting oil into the pore space using a Harvard Apparatus Pump 11 Elite syringe pump, injecting ≈ 30 pore volumes (PVs) at a fixed volumetric flow rate $Q_{nw} = 15$ mL/h; here, the number of PVs injected after a duration t is given by $Q_{nw}t/(\phi_0 A\ell)$. We simultaneously acquire tiled images spanning the entire cross section of the medium successively. Because the oil is undyed, it appears dark in the confocal micrographs, as indicated in the top of Fig. 1(b). Thus, comparing the micrographs to those obtained during initial characterization of the pore structure provides a 2D map of the oil configurations at subpore resolution. Due to the high flow rate Q_{nw}, oil saturates the majority of the pore space. The measured residual oil saturation S_{OR}, defined as the fraction of the pore space area occupied by oil, is 0.75. We normalize all subsequent measurements of S_{OR} by this maximal value, as indicated by the first data point in Fig. 1(c).

We then reinject ≈ 55 PVs of the particle-free wetting fluid at a rate of $Q_w = 0.15$ mL/h, emulating flow conditions in many subsurface formations [34]; in this case, PV $\equiv \int_0^t Q/(A\ell\phi(t))dt$ and the time-dependent porosity $\phi(t)$ measured directly from the confocal micrographs accounts for the fraction of the pore space accessible to the wetting fluid, which changes as oil is mobilized from the porous medium. Under these conditions, the wetting fluid flow leads to the formation of discrete droplets, or ganglia, of the nonwetting oil. While some of these ganglia become mobilized by the wetting fluid, $\approx 72\%$ of the original oil in place remains trapped by capillarity [33,35], as indicated by the decrease in S_{OR}, shown by the black circles in Fig. 1(c), within the first ≈ 6 PVs of fluid injection. The wetting fluid then continues to flow around them. This protocol thus establishes an initial steady-state configuration of trapped ganglia, as indicated by the circles for ≈ 6–50 PVs in Fig. 1(c) and exemplified by the micrograph in Fig. 1(d). As is frequently the case in confined and stratified media [36,37], most of the trapped ganglia are located near the boundaries of the medium, with smaller ganglia closer to the center of the pore space.

III. MOBILIZATION OF TRAPPED OIL BY COLLOIDAL PARTICLES

To explore whether and how colloidal particles can help mobilize the trapped oil, we next inject a suspension of positively charged, amine-terminated polystyrene particles (Sigma Aldrich) of diameter $d_p = 1$ μm into the medium. The particles are fluorescently labeled, with primary excitation and emission at 470 and 505 nm, respectively; these values are distinct from those of the wetting fluid, enabling multiplexed imaging of both particles and wetting fluid simultaneously. The spatial resolution of the imaging is 3 μm, and thus, each pixel comprises up to three particles. We first homogenize a concentrated 2.5 vol% aqueous suspension of the particles by sonicating for 10–15 min, and then redisperse the particles in the wetting fluid at a concentration of 8×10^{-3} vol%. We then inject this suspension into the porous medium directly following the particle-free wetting fluid injection, at the same flow rate $Q_w = 0.15$ mL/h. The initiation of particle injection is indicated by the arrow in Fig. 1(c). As injection progresses, the particles gradually deposit onto the negatively charged glass matrix throughout the medium due to electrostatic attraction [38], indicated by the red in Fig. 1(e). The measured solid area fraction averaged over the entire medium, $1 - \phi(t)$, increases due to deposition and eventually plateaus after ≈ 40 PVs of the suspension are injected, as shown by the gray squares in Fig. 1(c), likely due to electrostatic repulsion between like-charged particles [38].

By constricting the pore space, this process of deposition is usually thought to detrimentally hinder fluid flow. Unexpectedly, however, we find that trapped ganglia are concomitantly mobilized from the medium: the residual oil saturation decreases as deposition progresses, ultimately reaching only $\approx 30\%$ of its initial steady-state value after ≈ 30 PVs of suspension are injected, as shown by the black circles for ≈ 50–80 PVs in Fig. 1(c) and exemplified by the micrograph in Fig. 1(e). Clearly, particle deposition promotes, not hinders, trapped oil mobilization.
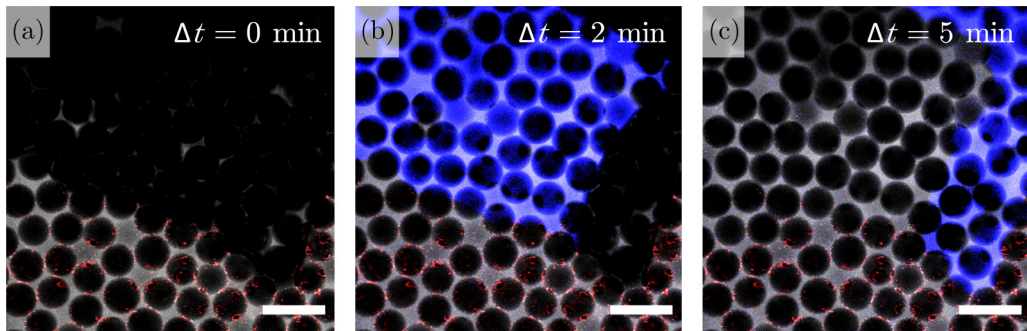
FIG. 2. Oil mobilization does not occur due to colloidal surface activity. Magnified views of confocal micrographs show an oil ganglion (a) before, (b) during, and (c) after mobilization. White regions show pore space, black circles show the bead matrix, additional black regions show oil, with the additional red showing colloidal particles. Some particles appear inside the ganglion due to the non-zero optical slice thickness. Particles are deposited on the bead surfaces, but do not localize at the ganglion surface, indicating that they are not surface active. Blue regions in (b) and (c) show portions of the ganglion that are mobilized between (a)–(b) and (b)–(c). Scale bars represent 250 μm. Imposed flow direction is from left to right.

IV. PARTICLE DEPOSITION CHARACTERISTICS

Why does particle deposition promote oil mobilization? Two possible mechanisms are (i) colloidal surface activity, which reduces the fluid-fluid interfacial tension and thereby reduces the strength of capillarity keeping ganglia trapped, and (ii) selective clogging of some pores redirecting the fluid flow toward trapped ganglia. We use our pore-scale visualization to examine the influence of these mechanisms in our experiment.

We first consider the possibility that the particles are surface active and localize at the ganglia surfaces. Previous studies of polystyrene colloids indicate that amine-functionalized particles are only weakly surface active at equilibrium [39,40], suggesting that this mechanism for ganglion mobilization is unlikely. This suggestion is confirmed by direct inspection of the distribution of particles during ganglion mobilization. We do not observe particle localization at the ganglia surfaces, as exemplified in Fig. 2. The dark region in the top of Fig. 2(a) shows a portion of the ganglion immediately before it is mobilized; notably, the particles, shown by the red dots, deposit on the surrounding glass bead matrix, but do not noticeably localize at the ganglion surface. This feature is also apparent in Fig. 2(b), which shows the ganglion in black as it is mobilized, with the portion of the ganglion that has been mobilized in this time step shown in blue; the boundary of this mobilized region is distinctly particle-free. We observe the same lack of particle localization in Fig. 2(c), which shows the ganglion immediately after it has been mobilized from the field of view, with the remaining portion of the ganglion that has been mobilized shown in blue. The ganglion is mobilized as particles are deposited onto the surrounding bead matrix; however, we again do not observe any particle localization at the boundary of the mobilized region. Thus, mobilization of trapped oil is not due to colloidal surface activity.

Next, we consider the possibility of flow redirection as a result of pore clogging. In particular, as particles deposit on the bead matrix, they may constrict and even occlude tight constrictions, possibly redirecting subsequent flow through the pore space. However, previous studies indicate that this behavior requires a considerable amount of deposition [41,42], which is unlikely to occur given the dilute volume fraction of particles ($<10^{-2}$ vol%) used in our experiment and the limited overall duration of particle injection. Indeed, as previously determined using experiments on single pores [41], the total number of particles that must flow through each pore to clog it, N^*, can be estimated using the empirical scaling relation $N^* \approx 5,000(2a_t/d_p)^4$, where $2a_t$ and d_p are the diameter of a pore constriction (a throat) and a particle, respectively. In our experiment, $a_t \approx 0.16a = 11$ μm

[43,44] and $d_p = 1\ \mu$m, yielding a threshold number of particles required to clog each pore, $N^* \approx 1 \times 10^9$. By contrast, the characteristic number of particles that flow through each pore over the entire experimental duration, calculated using the imposed flow rate $Q_w = 0.15$ mL/h, the maximal amount of time during which particles flow through the system $t \approx 10$ h, the number of pore volumes of particle suspension flowed over that time PVs $\approx$65, the suspension volume fraction of 8×10^{-3} vol%, and the individual particle diameter of 1 μm—is $N_{\text{tot}} \approx 4 \times 10^8$, much smaller than the estimated N^*. Moreover, the number of particles that flow through each pore before the onset of oil mobilization is even smaller than this value. Thus, clogging is not likely to occur in our experiment.

This expectation is again confirmed by direct inspection of the distribution of particles during ganglion mobilization: we do not observe pore clogging or strong variations in deposition in the different pores away from trapped ganglia, as exemplified by the micrograph shown in Fig. 1(e), as well as the magnified views of ganglia mobilization shown in Figs. 2 and 3. The dark region in the top of Fig. 3(a) again shows a portion of a ganglion immediately before it is mobilized; in this case, the ganglion is still trapped in the porous medium 2 h, or after 13 PVs of further fluid injection, after that shown in Fig. 2 is mobilized, resulting in more deposition on the surrounding beads. We again observe little to no particle localization at the ganglion surface, consistent with the results shown in Fig. 2. Notably, we do not observe appreciable variations in particle deposition from pore to pore, either along the flow direction or laterally. Furthermore, though they are increasingly constricted, the individual pores still permit fluid flow through them; particles only occupy <20% of the available pore space area, as shown by the gray points in Fig. 3(d) determined directly from the confocal micrographs. These features are also apparent in Figs. 3(b)–3(c), which again show mobilized portions of the ganglion in blue. After the ganglion at the top of the micrograph is mobilized, new particles are redeposited in its wake, shown by the additional red in the top region of Fig. 3(c), helping to even out the spatial variations in permeability. Indeed, during and well after mobilization, we again find that particle deposition is nearly uniform across pores, as shown by the maroon and red points in Fig. 3(d), consistent with previous findings [45]. Thus, mobilization of trapped oil is not due to selective clogging of pores.

Our visualization of particle deposition reveals that it constricts but does not clog pores throughout the medium and that the extent of oil mobilization is correlated with the extent of deposition. These observations hint at a different mechanism of oil mobilization. We hypothesize that deposition reduces the permeability of the medium, thereby enabling the viscous stresses exerted by the flowing wetting fluid on the trapped ganglia to overcome the influence of capillarity keeping ganglia trapped. To test this hypothesis, we use our micrographs to estimate the permeability reduction, thereby providing an estimate of how the local viscous stresses are modified, as detailed in the following section.

V. PERMEABILITY REDUCTION BY COLLOIDAL DEPOSITION

To accomplish this goal, we first establish the connection between the position- and time-dependent porosity of the medium, $\phi(x, t)$, and the thickness of the layer of particles deposited on the bead matrix, $\varepsilon(x, t)$; here, x is the position along the imposed flow direction as indicated in Fig. 1(a) and both quantities are averaged laterally over the y direction. In our experiment, we acquire data at a single z location and assume that ϕ and ε are uniform in the z direction, since the medium is randomly packed and previous experiments and simulations have shown the flow to be statistically uniform throughout [46,47].

Our pore-scale visualization of deposition shown in Figs. 2, 3, and 4(a) indicates that particles are deposited in thin, nearly uniform layers around the spherical glass beads. We rationalize this uniform pore-scale deposition profile by calculating the particle Péclet number, which describes the ratio of advective to diffusive transport, Pe $\equiv (Q_w/A)/(\mathscr{D}/d_p)$, where Q_w is the imposed flow rate, A is the cross-sectional area of the porous medium, $\mathscr{D}$ is the particle diffusivity, and d_p is the particle diameter. We calculate $\mathscr{D}$ using the Stokes-Einstein equation, $\mathscr{D} = k_B T / 3\pi \mu_w d_p$, where k_B is Boltzmann's constant and $T = 300$ K is the temperature of the fluid, yielding Pe ≈ 100 for
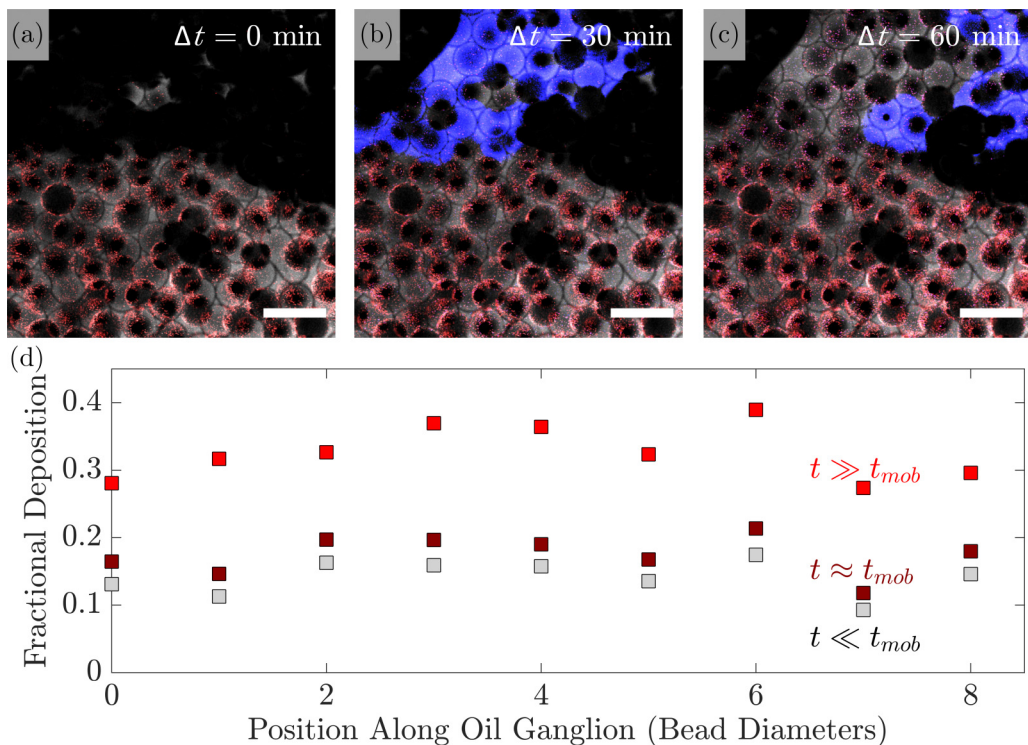
FIG. 3. Oil mobilization does not occur due to selective clogging of pores driving flow redirection. Magnified views of confocal micrographs show an oil ganglion (a) before, (b) during, and (c) after mobilization. White regions show pore space, black circles show the bead matrix, additional black regions show oil, with the additional red showing colloidal particles. Some particles appear inside the ganglion due to the nonzero optical slice thickness. The appearance of glass beads that are not completely black and have a shaded outline is a result of imperfect index matching between the wetting fluid and the beads. Particles are uniformly deposited on the bead surfaces both along and transverse to the ganglion; we do not observe selective clogging of pores. Blue regions in (b) and (c) show portions of the ganglion that are mobilized between (a)–(b) and (b)–(c). Scale bars represent 250 μm. Imposed flow direction is from left to right. (d) Data showing the fraction of the pore space immediately transverse to the ganglion that is occupied by deposited particles, measured using the confocal micrographs at three different times. Gray points correspond to (a), maroon points correspond to (b), and red points correspond to the end of the experiment, shown in Fig. 1(e). In all cases, the deposition is uniform across pores.

our experiment. While this calculation indicates that advective transport by the mean flow slightly dominates over diffusive transport of single particles, it does not fully capture the complicated flow in a porous medium. Previous measurements indicate that the flow velocities deviate strongly from the mean, in many cases being much smaller [48], particularly upstream of each bead [49], potentially leading to uniform deposition around the beads. This expectation has been confirmed in recent experiments investigating polystyrene particle transport in glass bead packings, which reveal that the interplay between particle interactions and flow limit deposition on the upstream faces of the beads and promote uniform deposition around each bead surface, even at Pe $\gtrsim$ 100 [50]. Thus, for simplicity, we approximate deposition at the pore scale to be uniform around the individual beads, with a deposition thickness ε, as schematized in Fig. 4(b). This thickness is then given by

$$\varepsilon(x,t) \approx a\left[\left(\frac{1 - \phi(x,t)}{1 - \phi_0}\right)^{1/3} - 1\right], \qquad (1)$$
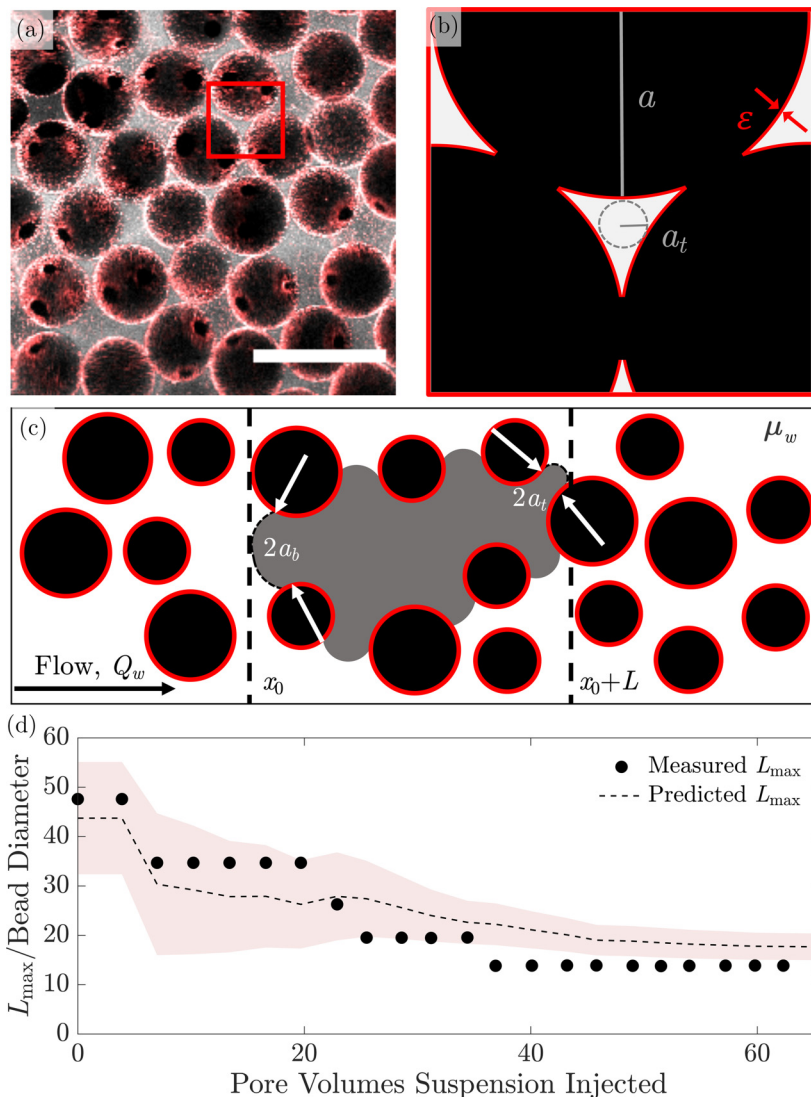
FIG. 4. Permeability reduction due to colloidal deposition promotes oil mobilization. (a) Magnified view of a confocal micrograph of colloidal deposition. White regions show pore space, black circles show the bead matrix, additional black regions show trapped oil ganglia, with the additional red showing deposited colloidal particles. Small black circles in the beads show the particle-free contacts between adjacent beads. Scale bar represents 250 μm. Imposed flow direction is from left to right. Deposition is nearly uniform over each bead surface. (b) Schematic of a pore throat of radius a_t, showing a uniform layer of deposited particles of thickness ε. (c) Schematic of a trapped oil ganglion. The grains that comprise the porous medium are shown black with red outlines to indicate deposition. The pore body and pore throat diameters, $2a_b$ and $2a_t$, are indicated at the upstream and downstream ends of the trapped ganglion at the positions x_0 and $x_0 + L$ along the flow direction, respectively. We also indicate the wetting fluid flow rate, Q_w, with directionality from left to right and a constant viscosity, μ_w. (d) Confocal measurements of the maximal length along the flow direction of trapped ganglia, $L_{\max}$, over the course of colloidal injection. The initial point corresponds to Fig. 1(d). As deposition progresses, increasingly smaller ganglia are mobilized from the medium, indicated by the decrease in the measured $L_{\max}$. Dashed line shows our theoretical prediction of $L_{\max}$ from Eqs. (6) and (7). The red region shows uncertainty in the prediction arising from heterogeneities in deposition, calculated from $\pm$ the standard deviation in the measured ϕ over the medium.

where ϕ_0 is the initial porosity before particle injection. We obtain $\phi(x, t)$ for the oil-free regions of the medium directly from the confocal micrographs using adaptive binarization, restricting all analysis to ≈ 5 bead diameters away from the inlet and outlet to minimize the influence of boundaries. Moreover, to reduce noise, we smooth the porosity measurements by segmenting the porous medium into representative elementary volumes (REV) ≈ 10 bead diameters in length, following common practice [51]. This level of smoothing provides a coarse-grained approach that results in a more realistic permeability estimate, but maintains enough fine-grained detail to incorporate any variations in deposition along the length of the medium. We thereby obtain $\varepsilon(x, t)$, which ranges from 0 to ≈ 6 μm over the course of the experiment, from Eq. (1).

Next, we use $\phi(x, t)$ and $\varepsilon(x, t)$ to estimate the permeability, $k(x, t)$, of the oil-free regions of the medium. Because ε is more than an order of magnitude smaller than a, we do this by modifying the classic Kozeny-Carman model, which reasonably predicts the permeability of bead packings similar to those used in our experiment [32,52]. Specifically, following typical convention [53], we model the pore space as a parallel bundle of cylindrical tubes of hydraulic radius equal to that of a packing of beads of radius $a + \varepsilon$. As detailed in Appendix A, this model, along with Eq. (1), yields the relation

$$k(x, t) = \frac{a^2}{18\tau} \left(\frac{1 - \phi(x, t)}{1 - \phi_0} \right)^{2/3} \frac{\phi(x, t)^3}{[1 - \phi(x, t)]^2}, \tag{2}$$

where τ is the tortuosity of the pore space, assumed to be equal to 2 for simplicity [48]. This relation quantifies the intuition that as deposition progresses and ϕ decreases, k decreases as well. Thus, from our measurements of $\phi(x, t)$, we determine $k(x, t)$ via Eq. (2).

VI. MODEL FOR DEPOSITION-INDUCED MOBILIZATION

How does a deposition-induced reduction in permeability promote oil mobilization? To answer this question, we examine the competition between the viscous stress exerted by the flowing wetting fluid on a ganglion and the capillary pressure threshold that must be overcome to displace the ganglion. The gradient in the wetting fluid pressure P_v is given by Darcy's law: $\frac{\partial P_v}{\partial x} = \frac{\mu_w(Q_w/A)}{\kappa k(x,t)}$, where the relative permeability κ is an empirical parameter $\leqslant 1$ used to quantify the modified transport through the medium due to the presence of trapped oil [51]. The viscous pressure drop ΔP_v across a ganglion of length L along the imposed flow direction and with upstream end located a distance x_0 from the inlet can then be approximated as

$$\Delta P_v \approx \frac{\mu_w(Q_w/A)}{\kappa} \int_{x_0}^{x_0+L} \frac{dx}{k(x, t)}, \tag{3}$$

where the ganglion spans $x_0 \leqslant x \leqslant x_0 + L$ as schematized in Fig. 4(c). To mobilize the ganglion, this viscous pressure drop must be large enough to squeeze the ganglion through the pores of the medium. Specifically, the ganglion must displace the wetting fluid from a downstream pore, requiring it to overcome the capillary pressure threshold $2\gamma \cos\theta/a_t$, where a_t is the radius of the downstream pore constriction, known as a throat, schematized in Fig. 4(b). The ganglion must also be displaced by the wetting fluid from an upstream pore, requiring the capillary pressure within the pore to fall below the threshold $2\gamma \cos\theta/a_b$, where a_b is the radius of the upstream pore, known as a body. Thus, to mobilize a ganglion from the medium, ΔP_v must exceed the capillary pressure threshold

$$\Delta P_c \approx 2\gamma \cos\theta \left[\frac{1}{a_t(x_0, t)} - \frac{1}{a_b(x_0 + L, t)} \right]. \tag{4}$$

In previous studies, increasing the viscous stresses on ganglia was accomplished by increasing the wetting fluid flow rate, Q_w, to promote mobilization [33]. Here, we examine another way of increasing these viscous stresses: by depositing particles in the pore space and thereby locally reducing permeability.

In the particle-free case, k, a_t, and a_b are independent of position and time; Eq. (3) then reduces to $\Delta P_v \approx \mu_w(Q_w/A)L/(\kappa k_0)$, with the pristine medium permeability k_0 given by substituting $\phi = \phi_0$ into Eq. (2), and Eq. (4) reduces to $\Delta P_c \approx 2\gamma \cos\theta(1/a_t - 1/a_b)$. As a simplifying first step—motivated by the fact that our bead packings are comprised of beads with a narrow distribution of sizes—we adopt a mean-field approach for the pristine medium where a_t and a_b are averaged with $a_t \approx 0.16a$ and $a_b \approx 0.24a$ [43,44] instead of explicitly considering the pore-to-pore variation of the pore geometry. Ganglia are only mobilized if $\Delta P_v \geqslant \Delta P_c$, or equivalently, if their normalized length $\tilde{L}$ exceeds a threshold value

$$\tilde{L}_{\max} = \frac{\kappa k \cos\theta}{a \cdot \mathrm{Ca}}\left(\frac{1}{a_t} - \frac{1}{a_b}\right); \tag{5}$$

here, overtildes indicate ganglion lengths that have been normalized by the bead diameter $2a$ and the Capillary number, defined as $\mathrm{Ca} \equiv \mu_w(Q_w/A)/\gamma$, quantifies the competition between viscous and capillary stresses at the pore scale. This definition is based on the typical convention established in previous studies of flow through porous media [54,55]; it represents a global quantity defined using macroscopically imposed injection conditions, and in our experiment, $\mathrm{Ca} \approx 4 \times 10^{-6}$ is held constant. Previous permeability measurements performed in a similar porous medium using nearly identical fluids and flow conditions indicate that $\kappa \ll 0.1$ for the range of residual oil saturations explored here [33]. Furthermore, other relative permeability measurements suggest that κ varies only minimally in this range of oil saturations [56–59]. Therefore, for simplicity, we approximate the relative permeability as $\kappa \approx 0.02$—a value that is both consistent with these previous findings and yields the best fit to our data. Using these experimental values, we expect that before particle injection, all ganglia longer than $\tilde{L}_{\max} \approx 44$ are mobilized, eventually establishing the initial steady-state configuration of trapped oil shown for $\approx$6–50 PVs in Fig. 1(c) and exemplified by the micrograph in Fig. 1(d). Direct analysis of the confocal micrographs yields excellent agreement with this expectation: we find $\tilde{L}_{\max} = 48$ for this steady-state configuration in our experiment, as shown by the first data point in Fig. 4(d), with all larger ganglia being mobilized in the first $\approx$6 PVs of wetting fluid injection. Thus, oil mobilization in a particle-free medium can be quantitatively described through our balance of viscous and capillary stresses.

After particle injection is initiated, k, a_t, and a_b are no longer constant; $k(x,t)$ is given by Eq. (2), while $a_t(x,t) \approx 0.16a - \varepsilon(x,t)$ and $a_b(x,t) \approx 0.24a - \varepsilon(x,t)$, with $\varepsilon(x,t)$ given by Eq. (1). In this case, ganglia are again only mobilized if $\Delta P_v \geqslant \Delta P_c$, but now with ΔP_v and ΔP_c given by Eqs. (2) and (4), respectively. Thus, we expect that ganglia are mobilized when their length L exceeds a threshold value $L_{\max}$ given by the solution to the following integral equation:

$$\int_{x_0}^{x_0+L_{\max}} \frac{dx}{k(x,t)} = \frac{2\kappa\cos\theta}{\mathrm{Ca}}\left[\frac{1}{a_t(x_0+L_{\max},t)} - \frac{1}{a_b(x_0,t)}\right]. \tag{6}$$

This equation quantifies the intuition that as colloidal deposition progresses, permeability reduction in the medium increases the viscous stresses on ganglia, decreasing $L_{\max}$ and enabling increasingly smaller ganglia to be mobilized from the medium.

We again use our experimental measurements to test this prediction. Because particle deposition is nearly uniform throughout the medium, as shown in Figs. 1, 2, and 3, we average the values of $k(x,t)$ and $\varepsilon(x,t)$ predicted by Eqs. (2) and (1), respectively, over the entire medium; the averaged values are given by $\bar{k}(t) \equiv \ell^{-1}\int_0^\ell k(x,t)dx$ and $\bar{\varepsilon}(t) \equiv \ell^{-1}\int_0^\ell \varepsilon(x,t)dx$, respectively. Substituting these averages in Eq. (6) yields a more simplified prediction for the maximal length of a trapped ganglion:

$$\tilde{L}_{\max}(t) = \frac{\kappa\bar{k}(t)\cos\theta}{a \cdot \mathrm{Ca}}\left(\frac{1}{\bar{a}_t(t)} - \frac{1}{\bar{a}_b(t)}\right), \tag{7}$$

where $\bar{a}_t(t) \approx 0.16a - \bar{\varepsilon}(t)$ and $\bar{a}_b(t) \approx 0.24a - \bar{\varepsilon}(t)$. As before, $\mathrm{Ca} \approx 4 \times 10^{-6}$ and we choose $\kappa = 0.02$, based on previous measurements obtained for a similar experimental system [33], and

consistent with other studies [56–59]. Therefore, substituting the experimental values into Eq. (7), we expect that as particles are injected into the porous medium, all ganglia longer than $\tilde{L}_{\max}$ are mobilized, with $\tilde{L}_{\max}$ decreasing from ≈ 44 to ≈ 18 as deposition progresses, indicated by the dashed line in Fig. 4(d). That is, with increasing amounts of colloidal deposition, we expect that increasingly smaller ganglia can be mobilized from the medium. Direct analysis of the confocal micrographs again yields excellent agreement with this expectation: remarkably, we find that $\tilde{L}_{\max}$ decreases from 48 to 15 over the course of the experiment, as shown by the data points in Fig. 4(d), reaching the final steady state after ≈ 40 PVs of suspension are injected. Thus, the configurations of ganglia mobilized through colloidal deposition can be quantitatively described through our balance of viscous and capillary stresses.

The approach to steady state in Fig. 4(d) is strikingly similar to that shown by the black points in Fig. 1(c). Indeed, as a final test of our theory, we predict not just the maximal length of trapped ganglia, but the total amount of trapped oil, S_{OR}. We do this using our confocal micrographs by summing the pore space area occupied by all ganglia with lengths $\tilde{L}$ less than the $\tilde{L}_{\max}$ value predicted by Eq. (7), at each experimental time point. The predicted S_{OR} is shown by the dashed line in Fig. 1(c). We again observe excellent agreement between the measured and predicted S_{OR}; both decrease over the course of colloidal injection and deposition, ultimately leading to $S_{OR} \approx 20\%$ of its maximal value. Thus, the extent of deposition-induced oil mobilization can also be quantitatively described through our balance of viscous and capillary stresses.

VII. DISCUSSION

Our work reveals that particle deposition can promote mobilization of trapped oil ganglia from a porous medium. In particular, by reducing the local permeability, particle deposition increases the viscous stresses on ganglia, enabling them to overcome the influence of capillary stresses that keep them trapped. To identify the essential physics of this problem, our theory adopts a mean-field representation of the medium as a simplifying first step. Nevertheless, it yields predictions for the size and amount of mobilized fluid. Both of these quantities are in good agreement with the experimental measurements; however, incorporating spatial variations in pore geometry will be a useful next step that builds on the current work.

Furthermore, our analysis only describes the onset of ganglion mobilization, but does not consider subsequent ganglion dynamics. For example, we assume that as ganglia are mobilized, they do not interact with other ganglia as they traverse the porous medium, though coalescence is possible. As a result, ganglia that are smaller than the threshold predicted by our theory could be mobilized, potentially explaining the slight mismatch between our predicted values and measurements of the residual oil saturation at later times: specifically, our theory slightly overpredicts the measurements shown by the black points for ~ 80–100 injected PVs in Fig. 1(c). Additionally, it is possible that despite the strong attractive interactions between particles and glass beads, mobilized ganglia can remove some deposited particles via capillary forces. This removal would result in a temporary increase in local permeability until particles redeposit there; we then expect that after sufficient redeposition of particles, new ganglia can be mobilized, potentially enabling this process to repeat itself. This cyclic process could underlie the fluctuations in the overall amount of deposition measured at early times in our experiment, shown by the slight oscillations in the gray points for ~ 60–80 injected PVs in Fig. 1(c). It could also explain the slight mismatch between the predicted values and experimental measurements of the residual oil saturation at these times, shown by the dashed line and black points, respectively: because removal of particles through ganglion mobilization would result in a temporary increase in local permeability until particles redeposit there, mobilization of subsequent ganglia could be underpredicted by our theory, or could take longer than we predict. Elucidating these complex dynamics will be an important direction for future work.

Finally, we note that while our work has focused on the flow rate-controlled case, our model can also be modified to consider pressure-controlled flow. Unlike the flow rate-controlled case, spatially-uniform particle deposition under a constant pressure drop would not result in enhanced

mobilization: the flow rate would necessarily decrease to compensate for the decreased permeability, maintaining a constant pressure drop across the medium, a constant pressure gradient along the medium, and therefore, an unchanged viscous pressure drop across each trapped ganglion. However, even for the case of a constant imposed pressure drop, particle deposition may still induce mobilization of trapped oil in the case of spatially-nonuniform (i.e., localized) deposition. Our theory enables us to establish a similar criterion to that presented in Eq. (6) to predict mobilization under these circumstances, as detailed in Appendix B.

VIII. CONCLUSION

Colloidal deposition in porous media is often considered to be a critical problem or, at best, a nuisance for applications including groundwater remediation and enhanced oil recovery; the permeability reduction resulting from deposition is thought to detrimentally impede subsequent flow and particle transport. Our work reveals that colloidal deposition can in fact be harnessed to mobilize and remove trapped immiscible fluids from a porous medium. In particular, we find that through deposition, a dilute ($<10^{-2}$ vol%) suspension of particles can mobilize and remove an additional $\sim$70% of trapped fluid from a porous medium. Pore-scale visualization demonstrates that this mechanism of mobilization does not require colloidal surface activity or selective clogging of pores; instead, by reducing the local permeability, deposited particles increase the viscous stresses exerted on trapped fluid droplets by the surrounding fluid, enabling them to become mobilized. By analyzing the colloidal deposition profile and the pore-scale fluid stresses, we develop a geometric model that predicts which fluid droplets become mobilized, depending on their size [Eq. (6)], in excellent agreement with our experimental results. Furthermore, for a given starting distribution of trapped droplet sizes, this model enables us to predict the extent of fluid that is mobilized as deposition progresses, again in excellent agreement with our experimental results. The model can also be used to guide applications requiring a target amount of trapped fluid to be mobilized: given a desired value of S_{OR}, Eqs. (2) and (6) can be inverted to determine the extent of colloidal deposition required. Thus, in addition to shedding light on a new way by which colloids can mobilize trapped fluid from a porous medium, our work also provides quantitative guidelines for applying this mechanism. Because it does not require specialized physicochemical characteristics, we expect this mechanism could be utilized in diverse media of different structures, and applicable to colloids of differing chemistry and physical characteristics, including naturally occurring organic and inorganic colloids, e.g., fines.

APPENDIX A: MODEL FOR PERMEABILITY ALTERATION BY DEPOSITION

We model the pore space as a parallel bundle of cylindrical tubes of radius R and length $\ell' > \ell$, where $(\ell'/\ell)^2$ is defined as the hydrodynamic tortuosity τ. The mean flow speed in each tube, $\langle v \rangle$, is then given by the Hagen-Poiseuille equation:

$$\langle v \rangle \equiv \frac{Q}{\phi A} = \frac{R^2 \Delta P}{8 \mu_w \ell'}, \tag{A1}$$

where Q is the imposed volumetric flow rate through the entire medium, A is the cross-sectional area of the medium, ϕ is the medium porosity, and ΔP is the pressure drop across the entire medium. This mean flow speed is also given by Darcy's law:

$$\langle v \rangle \equiv \frac{Q}{\phi A} = \frac{k \Delta P}{\phi \mu_w \ell}, \tag{A2}$$

where k is the overall permeability of the medium. Equating Eqs. (A1) and (A2) thus yields a general expression for the permeability:

$$k = \frac{\phi R^2}{8 \tau}. \tag{A3}$$

Following typical convention [53], we solve for R by equating the hydraulic radii R_h of the tube bundle and the porous medium composed of beads of radius $a + \varepsilon$. For the tube bundle, this quantity is given by the ratio between the pore space cross section and the wetted perimeter, $R_h = \frac{\pi R^2}{2\pi R} = R/2$. For the porous medium, this quantity is given by the ratio between the pore space volume and the wetted surface area, $R_h = \frac{\phi A \ell}{N \times 4\pi (a+\varepsilon)^2}$, where $N = \frac{(1-\phi)A\ell}{\frac{4}{3}\pi(a+\varepsilon)^3}$ is the number of beads in the medium. Thus, equating both expressions for R_h yields

$$R = \frac{2\phi(a+\varepsilon)}{3(1-\phi)}. \tag{A4}$$

Finally, substituting Eq. (A4) into Eq. (A3), and applying Eq. (1) from the main text, yields our generalized prediction of the permeability, Eq. (2).

To highlight the impact of permeability reduction on enhanced mobilization, we contrast a porous medium in which particle deposition alters the porosity to that of a medium in which the pores have simply become uniformly smaller. If we consider the case of a pristine porous medium with smaller pores, the viscous pressure drop across a trapped ganglion of length L, given by $\Delta P_v \propto L/k$, is larger because k scales as a^2, where a is the bead radius. However, it is important to note here that the capillary pressure threshold that must be overcome to mobilize the ganglion, given by $\Delta P_c \propto 1/a$, is also larger in a medium with smaller pores. Balancing the two confirms that the normalized threshold ganglion length, $L_{\max}/2a$, is a constant and is thus unchanged when pore size is reduced, as one may expect. However, in the case of a porous medium in which particle deposition has altered both the effective grain size a and the porosity ϕ, the permeability decreases more than the capillary pressure threshold due to its dependence on porosity. The capillary pressure threshold increases as $1/(a + \varepsilon)$; however, this increase is not sufficient to overcome the increase in the viscous pressure drop due to the decrease in permeability, which decreases as $(a + \varepsilon)^2 \phi^3/(1 - \phi)^2$. Specifically, $\Delta P_v \propto \frac{L}{(a+\varepsilon)^2} \frac{(1-\phi)^2}{\phi^3}$ and $\Delta P_c \propto a/(a+\varepsilon)$; balancing the two in this case yields a normalized threshold ganglion length $\frac{L_{\max}}{2(a+\varepsilon)} \propto \frac{\phi^3}{(1-\phi)^2}$ that is not a constant, but also reduces when porosity is reduced.

APPENDIX B: THEORY FOR PRESSURE-CONTROLLED FLOW

To modify our theory for the case of a constant imposed pressure drop, ΔP, we consider both uniform and nonuniform deposition of particles along the flow direction. Though we do not expect to see enhanced mobilization in the case of uniform particle deposition under a constant imposed pressure drop, particle deposition may still induce mobilization in the case of nonuniform (i.e., localized) deposition. An example is sketched in Fig. 5. Here, we contrast a uniform deposition profile (black curves) under a constant total pressure drop across the medium, ΔP_t, with a nonuniform deposition profile in which more particles are deposited near the inlet of the medium (red curves). The corresponding permeability curves, k/k_0, where k_0 is the permeability of the pristine medium, are shown in the bottom panel of the figure; uniform deposition corresponds to a uniform k along
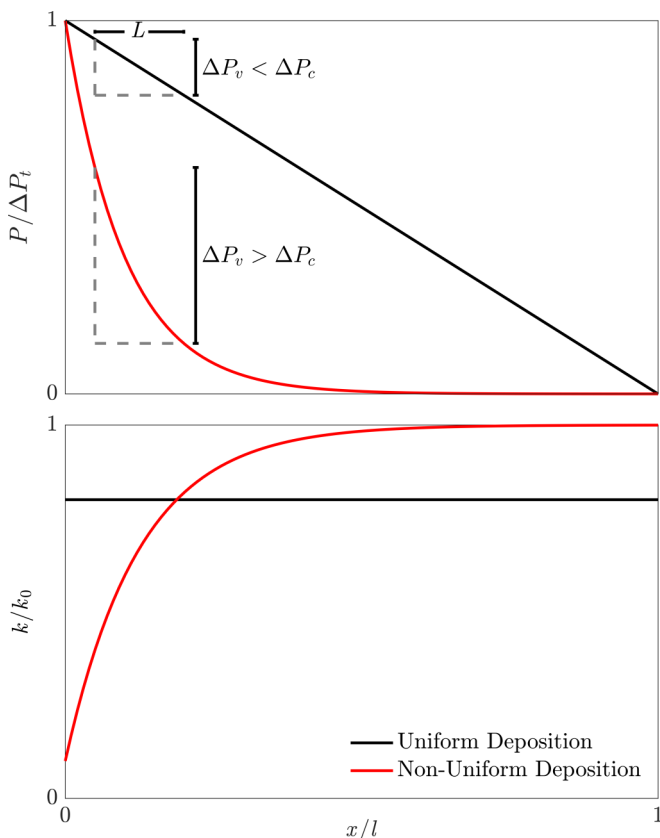
FIG. 5. Nonuniform deposition promotes mobilization under constant pressure drop ΔP_t. (top) Fluid pressure normalized by the pressure drop ΔP_t. A ganglion of length L has $\Delta P_v < \Delta P_c$ when particle deposition is spatially uniform at a low fixed ΔP_t (black). However, a nonuniform deposition profile obtained at the same constant ΔP_t can result in an increase of $\Delta P_v > \Delta P_c$ (red). (bottom) The corresponding profiles of normalized permeability, k/k_0, are shown over the length of the porous medium, x/ℓ.

the medium (black curve), while nonuniform deposition results in lower k near the inlet (red curve), where x is the position along the medium and ℓ is its length. The resultant variation of the fluid pressure $P/\Delta P_t$ along the porous medium is shown by the plot in the top panel.

In the case of uniform deposition at constant ΔP_t, the flow rate Q decreases concomitantly with increasing deposition. As a result, the viscous stress over a ganglion would not vary considerably, and thus new ganglia are not likely to be mobilized once deposition begins. An example of a ganglion of length L is shown by the horizontal dashed line in the top panel of the figure; the vertical bar indicates the viscous pressure drop across it, ΔP_v, which in this case is not sufficient to exceed the capillary pressure drop ΔP_c, and it remains trapped. As uniform deposition progresses, this viscous pressure drop does not change, and the ganglion still remains trapped. However, in the case of a nonuniform deposition profile, due to the nonuniform pressure gradient along the medium, the viscous pressure drop along the same ganglion is much larger and exceeds ΔP_c, as indicated by the lower vertical bar. In this case, the ganglion becomes mobilized. Thus, even in pressure-controlled flow, particle deposition can induce mobilization when it is nonuniform.

While our experiments focus on the flow-controlled case, our theoretical analysis can be adopted to model the case of mobilization under pressure-controlled flow due to nonuniform deposition.

Specifically, Eq. (3) of our paper would then be modified to be:

$$\Delta P_v = \frac{\mu_w}{A} \int_{x_0}^{x_0+L} \frac{Q_w(x,t)}{k'(x,t)} dx, \tag{B1}$$

where $k'(x,t) = \kappa(x,t)k(x,t)$. Here, we have two unknowns, Q and k'. However, we also have another relationship that comes from the overall constant pressure drop criterion as follows:

$$\Delta P_t = \text{const.} = \frac{\mu_w}{A} \int_0^\ell \frac{Q_w(x,t)}{k'(x,t)} dx. \tag{B2}$$

Using these modified equations in conjunction with Eq. (4) in the main text of the paper would then provide a modified criterion for ganglion mobilization via particle deposition under a constant imposed pressure drop.

---

[1] N. Bizmark, J. Schneider, E. de Jong, and S. S. Datta, Chapter 9: Transport of polymer colloids in porous media, *Polymer Colloids: Formation, Characterization and Applications*, pp. 289–321 (The Royal Society of Chemistry, London, 2020).

[2] T. Phenrat, N. Saleh, K. Sirk, R. D. Tilton, and G. V. Lowry, Aggregation and sedimentation of aqueous nanoscale zerovalent iron dispersions, Environ. Sci. Technol. **41**, 284 (2007).

[3] T. Phenrat, F. Fagerlund, T. Illangasekare, G. V. Lowry, and R. D. Tilton, Polymer-modified Fe^0 nanoparticles target entrapped NAPL in two dimensional porous media: Effect of particle concentration, NAPL saturation, and injection strategy, Environ. Sci. Technol. **45**, 6102 (2011).

[4] L. Hendraningrat, S. Li, and O. Torsæter, A coreflood investigation of nanofluid enhanced oil recovery, J. Pet. Sci. Eng. **111**, 128 (2013).

[5] F. Hussain, A. Zeinijahromi, P. Bedrikovetsky, A. Badalyan, T. Carageorgos, and Y. Cinar, An experimental study of improved oil recovery through fines-assisted waterflooding, J. Pet. Sci. Eng. **109**, 187 (2013).

[6] H. Zhang, A. Nikolov, and D. Wasan, Enhanced oil recovery (EOR) using nanoparticle dispersions: Underlying mechanism and imbibition experiments, Energy Fuels **28**, 3002 (2014).

[7] U. S. McKnight, S. G. Funder, J. J. Rasmussen, M. Finkel, P. J. Binning, and P. L. Bjerg, An integrated model for assessing the risk of TCE groundwater contamination to human receptors and surface water ecosystems, Ecol. Eng. **36**, 1126 (2010).

[8] H. H. Russell, J. E. Matthews, and G. W. Sewell, TCE removal from contaminated soil and groundwater, EPA Environmental Engineering Sourcebook, Report No. EPA/540/S-92/002, Environmental Protection Agency, Washington, DC, US, Office of Solid Waste and Emergency Response, 1991, p. 87.

[9] D. M. Mackay, P. V. Roberts, and J. A. Cherry, Transport of organic contaminants in groundwater, Environ. Sci. Technol. **19**, 384 (1985).

[10] M. Y. Corapcioglu and S. Jiang, Colloid-facilitated groundwater contaminant transport, Water Resour. Res. **29**, 2215 (1993).

[11] S. B. Roy and D. A. Dzombak, Chemical factors influencing colloid-facilitated transport of contaminants in porous media, Environ. Sci. Technol. **31**, 656 (1997).

[12] L. W. de Jonge, C. Kjærgaard, and P. Moldrup, Colloids and colloid-facilitated transport of contaminants in soils: An introduction, Vadose Zone J. **3**, 321 (2004).

[13] N. C. Wardlaw and J. P. Cassan, Oil recovery efficiency and the rock-pore properties of some sandstone reservoirs, Bull. Can. Petrol. Geol. **27**, 117 (1979).

[14] B. A. Suleimanov, F. Ismailov, and E. Veliyev, Nanofluid for enhanced oil recovery, J. Pet. Sci. Eng. **78**, 431 (2011).

[15] A. Roustaei and H. Bagherzadeh, Experimental investigation of SiO_2 nanoparticles on enhanced oil recovery of carbonate reservoirs, J. Pet. Explor. Prod. Technol. **5**, 27 (2015).

[16] B. Wei, Q. Li, F. Jin, H. Li, and C. Wang, The potential of a novel nanofluid in enhancing oil recovery, Energy Fuels **30**, 2882 (2016).

[17] R. Li, P. Jiang, C. Gao, F. Huang, R. Xu, and X. Chen, Experimental investigation of silica-based nanofluid enhanced oil recovery: The effect of wettability alteration, Energy Fuels **31**, 188 (2017).

[18] A. Franzetti, P. Caredda, C. Ruggeri, P. La Colla, E. Tamburini, M. Papacchini, and G. Bestetti, Potential applications of surface active compounds by *Gordonia* sp. strain BS29 in soil remediation technologies, Chemosphere **75**, 801 (2009).

[19] A. Franzetti, E. Tamburini, and I. M. Banat, Applications of biological surface active compounds in remediation technologies, *Biosurfactants* (Springer, Berlin, 2010) pp. 121–134.

[20] O. A. Alomair, K. M. Matar, and Y. H. Alsaeed, Nanofluids application for heavy oil recovery, in *SPE Asia Pacific Oil & Gas Conference and Exhibition* (Society of Petroleum Engineers, Dallas, 2014).

[21] A. Ragab, M. Salem, and A. E. Hannora, A Comparative investigation of nano particle effects for improved oil recovery–experimental work, in *SPE Kuwait Oil and Gas Show and Conference* (Society of Petroleum Engineers, Dallas, 2015).

[22] M. Magro, S. Domeneghetti, D. Baratella, P. Jakubec, G. Salviulo, E. Bonaiuto, P. Venier, O. Malina, J. Tuček, V. Ranc, G. Zoppellaro, R. Zbořil, and F. Vianello, Colloidal surface active maghemite nanoparticles for biologically safe Cr^{VI} remediation: From core-shell nanostructures to pilot plant development, Chem. Eur. J. **22**, 14219 (2016).

[23] H. Yu, Y. He, P. Li, S. Li, T. Zhang, E. Rodriguez-Pin, S. Du, C. Wang, S. Cheng, C. W. Bielawski, S. L. Bryant, and C. Huh, Flow enhancement of water-based nanoparticle dispersion through microscale sedimentary rocks, Sci. Rep. **5**, 8702 (2015).

[24] K. Kondiparty, A. Nikolov, S. Wu, and D. Wasan, Wetting and spreading of nanofluids on solid surfaces driven by the structural disjoining pressure: Statics analysis and experiments, Langmuir **27**, 3324 (2011).

[25] F. Kuhnen, K. Barmettler, S. Bhattacharjee, M. Elimelech, and R. Kretzschmar, Transport of iron oxide colloids in packed quartz sand media: Monolayer and multilayer deposition, J. Colloid Interface Sci. **231**, 32 (2000).

[26] M. R. Wiesner, M. C. Grant, and S. R. Hutchins, Reduced permeability in groundwater remediation systems: Role of mobilized colloids and injected chemicals, Environ. Sci. Technol. **30**, 3184 (1996).

[27] C. Chen, A. I. Packman, and J.-F. Gaillard, Pore-scale analysis of permeability reduction resulting from colloid deposition, Geophysical Research Letters **35**, L07404 (2008).

[28] F. Civan, Non-isothermal permeability impairment by fines migration and deposition in porous media including dispersive transport, Transp. Porous Media **85**, 233 (2010).

[29] L. Hendraningrat, B. Engeset, S. Suwarno, S. Li, and O. Torsæter, Laboratory investigation of porosity and permeability impairment in Berea sandstones due to hydrophilic nanoparticle retention, in *International Symposium of the Society of Core Analysts held in Napa Valley, California, USA* (2013), Paper SCA2013-062, p. 1619.

[30] S. A. Bradford and S. Torkzaban, Colloid transport and retention in unsaturated porous media: A review of interface-, collector-, and pore-scale processes and models, Vadose Zone J. **7**, 667 (2008).

[31] W. Zhang, V. L. Morales, M. E. Cakmak, A. E. Salvucci, L. D. Geohring, A. G. Hay, J.-Y. Parlange, and T. S. Steenhuis, Colloid transport and retention in unsaturated porous media: Effect of colloid input concentration, Environ. Sci. Technol. **44**, 4965 (2010).

[32] A. T. Krummel, S. S. Datta, S. Münster, and D. A. Weitz, Visualizing multiphase flow and trapped fluid configurations in a model three-dimensional porous medium, AIChE J. **59**, 1022 (2013).

[33] S. S. Datta, T. Ramakrishnan, and D. A. Weitz, Mobilization of a trapped non-wetting fluid from a three-dimensional porous medium, Phys. Fluids **26**, 022002 (2014).

[34] G. Medici, L. West, and S. Banwart, Groundwater flow velocities in a fractured carbonate aquifer-type: Implications for contaminant transport, J. Contam. Hydrol. **222**, 1 (2019).

[35] A. Payatakes and M. M. Dias, Immiscible microdisplacement and ganglion dynamics in porous media, Rev. Chem. Eng. **2**, 85 (1984).

[36] R. Walker, C. Hofstee, J. Dane, and W. Hill, Surfactant enhanced removal of PCE in a nominally two-dimensional, saturated, stratified porous medium, J. Contam. Hydrol. **34**, 17 (1998).

[37] A. Lashanizadegan, S. Ayatollahi, and H. Kazemi, Experimental and theoretical investigation of LNAPL movement in stratified media during soil remediation, Environ. Technol. **28**, 743 (2007).

[38] N. Bizmark, J. Schneider, R. D. Priestley, and S. S. Datta, Multiscale dynamics of colloidal deposition and erosion in porous media, Sci. Adv. **6**, eabc2530 (2020).

[39] J.-W. Kim, D. Lee, H. C. Shum, and D. A. Weitz, Colloid surfactants for emulsion stabilization, Adv. Mater. **20**, 3239 (2008).

[40] T. Feng, D. A. Hoagland, and T. P. Russell, Assembly of acid-functionalized single-walled carbon nanotubes at oil/water interfaces, Langmuir **30**, 1072 (2014).

[41] H. M. Wyss, D. L. Blair, J. F. Morris, H. A. Stone, and D. A. Weitz, Mechanism for clogging of microchannels, Phys. Rev. E **74**, 061402 (2006).

[42] B. Dersoir, M. R. de Saint Vincent, M. Abkarian, and H. Tabuteau, Clogging of a single pore by colloidal particles, Microfluid. Nanofluid. **19**, 953 (2015).

[43] R. Al-Raoush and C. Willson, Extraction of physically realistic pore network properties from three-dimensional synchrotron X-ray microtomography images of unconsolidated porous media systems, J. Hydrol. **300**, 44 (2005).

[44] K. E. Thompson, C. S. Willson, C. D. White, S. Nyman, J. P. Bhattacharya, and A. H. Reed, Application of a new grain-based reconstruction algorithm to microtomography images for quantitative characterization and flow modeling, Technical Report SPE 95887, Naval Research Lab Stennis Space Center Marine Geoacoustics Division, 2008.

[45] G. Gerber, D. A. Weitz, and P. Coussot, Propagation and adsorption of nanoparticles in porous medium as traveling waves, Phys. Rev. Res. **2**, 033074 (2020).

[46] R. Kouri and J. Sohlo, Liquid and gas flow patterns in random packings, Chem. Eng. J. **61**, 95 (1996).

[47] H. Freund, T. Zeiser, F. Huber, E. Klemm, G. Brenner, F. Durst, and G. Emig, Numerical simulations of single phase reacting flows in randomly packed fixed-bed reactors and experimental validation, Chem. Eng. Sci. **58**, 903 (2003).

[48] S. S. Datta, H. Chiang, T. S. Ramakrishnan, and D. A. Weitz, Spatial Fluctuations of Fluid Velocities in Flow through a Three-Dimensional Porous Medium, Phys. Rev. Lett. **111**, 064501 (2013).

[49] A. Y. Huang, M. Y. Huang, H. Capart, and R.-H. Chen, Optical measurements of pore geometry and fluid velocity in a bed of irregularly packed spheres, Exp. Fluids **45**, 309 (2008).

[50] G. Gerber, M. Bensouda, D. A. Weitz, and P. Coussot, Self-Limited Accumulation of Colloids in Porous Media, Phys. Rev. Lett. **123**, 158005 (2019).

[51] M. J. Blunt, *Multiphase Flow in Permeable Media: A Pore-Scale Perspective* (Cambridge University Press, Cambridge, 2017).

[52] X. Garcia, L. T. Akanji, M. J. Blunt, S. K. Matthai, and J. P. Latham, Numerical study of the effects of particle shape and polydispersity on permeability, Phys. Rev. E **80**, 021304 (2009).

[53] J. Bear, *Dynamics of Fluids in Porous Media* (American Elsevier Publishing, Amsterdam, 1972).

[54] I. Chatzis, N. R. Morrow, H. T. Lim *et al.*, Magnitude and detailed structure of residual oil saturation, Soc. Pet. Eng. J. **23**, 311 (1983).

[55] N. R. Morrow, I. Chatzis, J. Taber *et al.*, Entrapment and mobilization of residual oil in bead packs, SPE Reservoir Eng. **3**, 927 (1988).

[56] R. Wygal, Construction of models that simulate oil reservoirs, Soc. Pet. Eng. J. **3**, 281 (1963).

[57] J. T. Bartley and D. W. Ruth, Experimental investigation of unsteady-state relative permeability in sand-packs, in *Society of Core Analysis Conference* (2001) paper SCA2013-062, Vol. 22, pp. 1–14.

[58] M. Ashrafi, Y. Souraki, and O. Torsaeter, Effect of temperature on athabasca type heavy oil–water relative permeability curves in glass bead packs, Energy Environ. Res. **2**, 113 (2012).

[59] B. Ghanbarian, M. A. Ioannidis, and A. G. Hunt, Theoretical insight into the empirical tortuosity-connectivity factor in the *Burdine-Brooks-Corey* water relative permeability model, Water Resour. Res. **53**, 10395 (2017).